A collocated finite volume scheme for high-performance simulation of induced seismicity in geo-energy applications

Novikov, A.; Voskov, D. V.; Khait, M.; Hajibeygi, H.; Jansen, J. D.

DOI
10.2118/203903-MS

Publication date
2021

Document Version
Final published version

Published in
Society of Petroleum Engineers - SPE Reservoir Simulation Conference 2021, RSC 2021

SPE-203903-MS

A Collocated Finite Volume Scheme for High-Performance Simulation of Induced Seismicity in Geo-Energy Applications

A. Novikov, D. V. Voskov, M. Khait, H. Hajibeygi, and J. D. Jansen, TU Delft

This paper was prepared for presentation at the SPE Reservoir Simulation Conference, available on-demand, 26 October 2021 – 25 January 2022. The official proceedings were published online 19 October 2021.

Abstract

We develop a collocated Finite Volume Method (FVM) to study induced seismicity as a result of pore pressure fluctuations. A discrete system is obtained based on a fully-implicit coupled description of flow, elastic deformation, and contact mechanics at fault surfaces on a fully unstructured mesh. The cell-centered collocated scheme leads to convenient integration of the different physical equations, as the unknowns share the same discrete locations on the mesh. Additionally, a multi-point flux approximation is formulated in a general procedure to treat heterogeneity, anisotropy, and cross-derivative terms for both flow and mechanics equations. The resulting system, though flexible and accurate, can lead to excessive computational costs for field-relevant applications. To resolve this limitation, a scalable parallel solution algorithm is developed and presented. Several proof-of-concept numerical tests, including benchmark studies with analytical solutions, are investigated. It is found that the presented method is indeed accurate, stable and efficient; and as such promising for accurate and efficient simulation of induced seismicity.

Introduction

Mechanical deformation of subsurface reservoirs plays a key role in safe and optimal operation of many geoenergy applications. Hydraulic fracturing is a direct application in which rock mechanics is at the core of the operation design. Gas production, as another example, often causes subsidence which in turn can initiate induced seismicity and serious damages to surface infrastructures. Moreover, in geothermal operations, the re-injection of cooler fluid causes stress changes which results in thermo-hydro-mechanical deformations and can activate faults (Buijze et al., 2019). Successful exploitation of these geo-energy resources depends highly on development of robust and efficient computational simulators for coupled hydro-thermo-mechanical processes.

Galerkin finite element methods have been employed by many researchers to investigate induced seismicity (Jha and Juanes, 2014; Garipov et al., 2016; Garipov and Hui, 2019). Mixed finite elements methods were also extensively developed to allow for more accurate geomechanics simulations (Arbogast et al., 1997; Phillips and Wheeler, 2007). To enhance convergence properties of the linear systems, weakly-imposed symmetry of the stress tensor in mixed finite element methods was also developed in Arnold et al. (2007) and then used in combination with multi-point stress approximation in Ambartsumyan et al. (2020).

Alternatively, the Finite Volume Method (FVM) has recently gained high interests to be employed for geomechanics and poromechanics simulations. The FVM has become an essential tool for flow and transport simulation due to its local conservation property. For mechanical deformation, however, the conservation property does not have the same importance. Nonetheless, the FVM is still an attractive choice beacuse it represents conservation laws (in integral form) more naturally. The FVM has been employed for mechanical problems in a staggered configuration (Deb and Jenny, 2017a; Sokolova et al., 2019) and collocated (Nordbotten, 2014; Berge et al., 2020; Terekhov and Tchelepi, 2020; Terekhov, 2020a). The resulting systems are non-symmetric, but can be made weakly symmetric as proposed in Keilegavlen and Nordbotten (2017).

Some authors (Deb and Jenny, 2017b; Garipov et al., 2018) use fixed-stress splitting algorithms (Settari and Mourits, 1998; Kim et al., 2011) to decouple mechanics and flow equations. These are a form of sequential implicit (SI) solution schemes and often lead to more efficient simulations than fully implicit (FI) simulation. However, sequential schemes introduce certain restrictions on time step sizes. On the other hand, FI schemes (Sokolova et al., 2019; Garipov et al., 2016, 2018; Garipov and Hui, 2019; Berge et al., 2020) provide unconditionally convergent solutions and are more robust and convenient approaches for investigation of complex multiphysical problems. FI and SI approaches were compared in the context of coupled thermo-compositional-mechanics simulation in Garipov et al. (2018).

Although the FI approach does not imply any restriction on time step size, it requires an efficient linear-equation solution strategy for high resolution models. One such strategy is to construct a preconditioner based on the idea of the SI approach. In White et al. (2016), the authors employ a fixed-stress splitting concept in a sparse approximation of the Schur complement in order to obtain a block-preconditioned solution strategy. Later this approach was combined with a constrained pressure residual (CPR) preconditioner to construct a robust and effective solution strategy for coupled multiphase flow and mechanics (Klevtsov et al., 2016).

In the current study, we develop a collocated FI multi-point FVM scheme for poromechanics simulation of faulted reservoirs, following the work of Terekhov and Tchelepi (2020); Terekhov (2020a). The scheme can be used to solve poromechanics problems on unstructured polyhedral grids with a minimum of degrees of freedom per cell. It is also capable to take into account material heterogeneity while preserving mass and momentum balances. We extend this scheme to take into account discontinuities in displacements at faults. Stick-slip behavior is governed by additional constraints at the contact embedded in the discretization.

The developed algorithms have been embedded into the open-source Delft Advanced Research Terra Simulator (DARTS). DARTS is a general purpose simulation platform for energy transition applications. It was successfully applied for modeling of advanced petroleum (Khait and Voskov, 2018a; Lyu et al., 2021a), geothermal (Khait and Voskov, 2018b; Wang et al., 2020) and CO_2 sequestration (Kala and Voskov, 2020; Lyu et al., 2021b) applications. This facilitates further extension of the proposed geomechanics model for modern energy-related industrial applications.

The paper is organized as follows. First, we present the governing equations for coupled flow and geomechanics. Then we develop the discrete system of equations, the coupled multi-point approximation, and the strategy to solve this system. Next, we perform validation against analytical and numerical approaches for pure elastic deformation. Thereafter, we study slip and stress profiles over a fault in different configurations. Through these proof-of-concept test cases, we assess the performance and applicability of the proposed simulation approach.

Governing Equations

Single-phase flow in deformable porous media is governed by a coupled system of momentum balance and fluid mass balance equations, i.e.,

$$\begin{cases} -\nabla \cdot \sigma = \mathrm{f}, \\ \frac{\partial}{\partial t}(\phi\, \rho) + \nabla \cdot (\rho \mathbf{v}) = f, \end{cases} \tag{1}$$

subject to the closure relations as defined in Coussy (2003):

$$\sigma - \sigma^0 = \mathbb{C} : (\varepsilon - \varepsilon^0) - (p - p^0)B, \tag{2}$$

$$\phi - \phi^0 = \frac{b - \phi^0}{K_s}(p - p^0) + b(\varepsilon_V - \varepsilon_V^0), \tag{3}$$

$$\varepsilon = \frac{\nabla \mathrm{u} + \nabla \mathrm{u}^T}{2}, \tag{4}$$

$$\mathbf{v} = -\frac{K}{\mu}(\nabla p - \rho g \nabla z), \tag{5}$$

$$\rho = \rho(p), \quad \mu = \mu(p), \tag{6}$$

where σ is the rank-two total stress tensor, **f** is a vector of volumetric forces, φ is porosity, ρ is fluid density, **v** is Darcy's velocity, f is a source (sink) of fluid mass, $\mathbb{C}$ is a rank-four stiffness tensor, B is a diagonal rank-two tensor of Biot coefficients b, p is pore pressure, **u** is a vector of displacements, K_s is the bulk modulus of the solid phase, ε is the rank-two strain tensor, $\varepsilon_V = \mathrm{tr}(\varepsilon)$ is the volumetric strain, K is the rank-two permeability tensor, μ is fluid viscosity, and g is acceleration of gravity. Furthermore, a superscript '0' denotes the reference state of a variable, i.e., $\sigma^0 = \sigma(\mathbf{u}^0, p^0)$, $\varphi^0 = \varphi(\mathbf{u}^0, p^0)$, $\varepsilon^0 = \varepsilon(\mathbf{u}^0, p^0)$. Equations (2) and (3) represent stress and porosity changes, equation (4) describes infinitesimal strains, and equation (5) is Darcy's equation. The fluid properties density and viscosity are functions of pressure, as stated in equation (6). All variables have been listed in the Nomenclature section at the end of the paper. Note that Biot's coefficient b is restricted to the interval $\varphi 0 < b \leq 1$ and that $b = 1$ represents the incompressible solid rock limit.

We denote vectors with bold font, and tensors of rank higher than two with script font. Scalars and rank-two tensors are denoted with Roman letters. We also use the following definitions for the total traction vector **F**, fluid flux q and displacement flux $\tilde{q}$ over an interface with unit normal **n**:

$$\mathbf{F} = -\mathbf{n}^T\left[\mathcal{C} : \frac{\nabla \mathbf{u} + \nabla \mathbf{u}^T}{2} - pB\right], \tag{7}$$

$$q = -\mathbf{n}^T\left[\frac{K}{\mu}(\nabla p - \rho g \nabla z)\right], \tag{8}$$

$$\tilde{q} = \mathbf{n}^T[B\mathbf{u}]. \tag{9}$$

Boundary conditions for the system of equations (1) can be written as

$$\begin{cases} \mathbf{n}^T(a_n \mathbf{u}_b + b_n \mathbf{F}_b) = r_n, \\ (I - \mathbf{n}\mathbf{n}^T)(a_t \mathbf{u}_b + b_t \mathbf{F}_b) = \mathbf{r}_t, \\ a_p p_b + \frac{b_p}{\mu} K \mathbf{n} \cdot \nabla p = r_p, \end{cases} \tag{10}$$

where $\mathbf{F}_b$ and p_b are traction and pore pressure at the boundary, respectively. In addition, a_n,b_n,a_t, b_t, a_p,b_p are coefficients that determine the magnitude of their corresponding boundary conditions, r_n,rt, r_p are the corresponding condition values. Expressions (10) can describe a broad range of possible boundary conditions including Dirichlet ($a_n = a_t = 1$, $b_n = b_t = 0$), distributed force loading ($a_n = a_t = 0$, $b_n = b_t = 1$), free boundary ($a_n = a_t = r_n = 0$, $b_n = b_t = 1$, rt = 0), and roller conditions ($a_n = b_t = 1$, $b_n = r_n = a_t = 0$, $\mathbf{r}_t = \mathbf{0}$) for mechanics; and Dirichlet ($a_p = 1$, $b_p = 0$) and Neumann ($a_p = 0$, $b_p = 1$) conditions for flow.

At the fault interfaces we consider a gap vector **g** that is equal to the jump of displacements over the contact $\mathbf{g} = \mathbf{u}^+ - \mathbf{u}^-$, where +/− denote a particular side of the fault. The conditions that are applied to the contact read

$$\begin{cases} \mathbf{n}^T\dot{\mathbf{g}} = 0, & \\ (I - \mathbf{n}\mathbf{n}^T)\left(\mathbf{F}' - \eta F'_N \frac{\mathbf{F}'}{|\mathbf{F}'|}\right) = \mathbf{0}, & \Phi \geq 0, \\ (I - \mathbf{n}\mathbf{n}^T)\dot{\mathbf{g}} = \mathbf{0}, & \Phi < 0, \end{cases} \tag{11}$$

where the magnitude of the normal projection and the tangential projection of the effective traction vector $\mathbf{F}' = -\mathbf{n}_T \mathbb{C}: (\varepsilon - \varepsilon^0)$ at the contact surface are, respectively, $F'_N = \mathbf{n}^T\mathbf{F}'$ and $\mathbf{F}'_T = (I - \mathbf{n}\mathbf{n}^T)\mathbf{F}'$. Here, η is the friction coefficient, while the Coulomb function $\Phi = |\mathbf{F}'_T| - \eta F'_N$ is used as a slip criterion. The vector $\dot{\mathbf{g}}$ represents the time derivative of gap vector. The first condition in (11) represents a non-penetration condition which prohibits opening. This implies that the gap vector only allows for tangential displacements and therefore becomes a slip vector. The second condition governs relaxation of tangential traction once slip occurs, and the third one sets the change of tangential gap (i.e. the slip) to zero if the slip criterion is not satisfied.

Numerical Scheme

In this section, we briefly describe the discretization scheme for the continuum domain first, and then introduce fracture/fault discontinuities.

Finite Volume Method

According to the FVM, the momentum balance and fluid mass balance (1) in integral form for the *i*-th cell can be stated as

$$V_i \begin{pmatrix} -\nabla t \mathbf{f}^{n+1} \\ (\widetilde{\phi}\rho)_i^{n+1} - (\widetilde{\phi}\rho)_i^n - \nabla t\, f_i^{n+1} \end{pmatrix} + \sum_j \delta_j \left[\rho_i^{n+1} \left(\tilde{q}^0\right)_{ij}^{n+1} - \rho_i^n \left(\tilde{q}^0\right)_{ij}^{n+1} + \Delta t \left(\frac{\mathbf{F}}{\rho q / \mu}\right)_{ij}^{n+1} \right] = \mathbf{0}, \tag{12}$$

where superscripts *n*, and *n* + 1 denote the variables taken from the current and next time step, respectively. Also, subscript *j* enumerates the interfaces of the *i*-th cell, Δ*t* is the time step size, V_i is the volume of *i*th cell, δ_j denotes the area of the *j*th interface, **F**, *q*, $\tilde{q}$ are defined in equations (7), (8), and (9), respectively. Moreover, $\widetilde{\phi} = \phi^0 + (p - p^0)(b - \phi^0)/K_s$ holds.

Continuous Local Problem

Equation (12) requires consistent discrete formulation for the tractions and fluid mass fluxes at interfaces.

Let us introduce the vector of unknowns $\mathbf{w} = \{\mathbf{u}, p\}$. By imposing the continuity of the unknowns and continuity of fluxes, i.e., tractions and fluid mass fluxes between 1st and 2nd neighbouring cells (Terekhov, 2020a), one obtains

$$\mathbf{w}_{\delta 1} = \mathbf{w}_1 + [\mathrm{I} \otimes (\mathbf{x}_\delta - \mathbf{x}_1)^T](\nabla \otimes \mathbf{w}_1) = \mathbf{w}_2 + [\mathrm{I} \otimes (\mathbf{x}_\delta - \mathbf{x}_2)^T](\nabla \otimes \mathbf{w}_2) = \mathbf{w}_{\delta 2}, \tag{13}$$

$$-[I \otimes \mathbf{n}^T] S_1 (\nabla \otimes \mathbf{u}_1) + p_{\delta 1} B_1 = -[I \otimes \mathbf{n}^T] S_2 (\nabla \otimes \mathbf{u}_2) + p_{\delta 2} B_2, \tag{14}$$

$$\left(\mathbf{u}_{\delta 1} - \mathbf{u}_{\delta 1}^0\right) \cdot \mathrm{B}_1 \mathbf{n} - \frac{\Delta t}{\mu} \nabla p_1 \cdot K_1 \mathbf{n} + \frac{\nabla t}{\mu} \rho g \nabla z \cdot K_1 \mathbf{n} = \left(\mathbf{u}_{\delta 2} - \mathbf{u}_{\delta 2}^0\right) \cdot \mathrm{B}_2 \mathbf{n} - \frac{\Delta t}{\mu} \nabla p_2 \cdot K_2 \mathbf{n} + \frac{\nabla t}{\mu} \rho g \nabla z \cdot K_2 \mathbf{n}, \tag{15}$$

where $\mathbf{w}_1$ and $\mathbf{w}_2$ are unknowns at the cell centers, $\mathbf{x}_1$ and $\mathbf{x}_2$ are the positions of the cell centers, $\mathbf{x}_\delta$ denotes the center of the interface, ⊗ stands for the Kronecker product, $I \otimes (\mathbf{x}_\delta - \mathbf{x}_1)_T$, $I \otimes (\mathbf{x}_\delta - \mathbf{x}_2)_T$ represent 4 × 12 matrices, $\nabla \otimes \mathbf{w}_1$, $\nabla \otimes \mathbf{w2}$ and $\nabla \otimes \mathbf{u}_1$, $\nabla \otimes \mathbf{u}_2$ are 12 × 1 and 9 × 1 vectors respectively, $S_1 = Y\, C_1 Y^T$, $S_2 = Y\, C_2 Y^T$ are 9 × 9 matrices where *C* denotes a 6 × 6 symmetric stiffness matrix in Voigt notation and where

$$Y^T = \begin{bmatrix} 1 & 0 & 0 & 0 & 0 & 0 & 0 & 0 & 0 \\ 0 & 0 & 0 & 0 & 1 & 0 & 0 & 0 & 0 \\ 0 & 0 & 0 & 0 & 0 & 0 & 0 & 0 & 1 \\ 0 & 0 & 0 & 0 & 0 & 1 & 0 & 1 & 0 \\ 0 & 0 & 1 & 0 & 0 & 0 & 1 & 0 & 0 \\ 0 & 1 & 0 & 1 & 0 & 0 & 0 & 0 & 0 \end{bmatrix}.$$

Below we will use the following decomposition

$$\nabla \otimes \mathbf{w}_i = [I \otimes \mathbf{n}]\mathrm{G}_i + \mathrm{G}_{\tau i}, \qquad \mathrm{G}_i = [I \otimes \mathrm{n}^T][\nabla \otimes \mathbf{w}_i], \qquad \mathrm{G}_{\tau i} = [I \otimes (I - \mathbf{n}\mathbf{n}^T)][\nabla \otimes \mathbf{w}_i], \tag{16}$$

$$\left[I \otimes \mathbf{n}^T\right]S_i = T_i\left[I \otimes \mathbf{n}^T\right] + \Gamma_i, \qquad T_i = \left[I \otimes \mathbf{n}^T\right]S_i\left[I \otimes \mathbf{n}\right], \qquad \Gamma_i = \left[I \otimes \mathbf{n}^T\right]S_i\left[I \otimes (I - \mathbf{n}\mathbf{n}^T)\right], \tag{17}$$

$$K_i\mathbf{n} = \lambda_i\mathbf{n} + \boldsymbol{\gamma}_i, \qquad \lambda_i = \mathbf{n}^T K_i \mathbf{n}, \qquad \boldsymbol{\gamma}_i = (I - \mathbf{n}\mathbf{n}^T)K_i\mathbf{n}, \tag{18}$$

$$\begin{aligned} &\mathbf{x}_\delta - \mathbf{x}_1 = r_1\mathbf{n} + (\mathbf{x}_\delta - \mathbf{y}_1), \quad r_1 = \mathbf{n}\cdot(\mathbf{x}_\delta - \mathbf{x}_1) > 0, \quad \mathbf{y}_1 = \mathbf{x}_1 + r_1\mathbf{n}, \\ &\mathbf{x}_1 - \mathbf{x}_\delta = r_2\mathbf{n} + (\mathbf{y}_2 - \mathbf{x}_\delta), \quad r_2 = \mathbf{n}\cdot(\mathbf{x}_2 - \mathbf{x}_\delta) > 0, \quad \mathbf{y}_2 = \mathbf{x}_2 + r_2\mathbf{n}, \end{aligned} \tag{19}$$

where subscripts i = 1,2 refer to the cells neighboring an interface, r_1 and r_2 are distances between the cell centers and the interface, $\mathbf{y}_1$, $\mathbf{y}_2$ are projections of the cell centers on the interface, T_1 and T_2 are 3 × 3 matrices, Γ_1 and Γ_2 are 3 × 9 matrices, while scalars λ_1 and λ_2 and vectors γ_1 and γ_2 provide co-normal decompositions of K_1 and K_2. The 4 × 1 vectors $\mathbf{G}_1$ and $\mathbf{G}_2$, and the 12 × 1 vectors $\mathbf{G}_{\tau 1}$ and $\mathbf{G}_{\tau 2}$ represent normal and tangential projections respectively of the gradients of the unknowns.

Using the introduced notation, the continuity of fluxes, represented in equations (14) and (15), can be written in the following coupled form

$$A_1\mathbf{w}_1 + Q_1\mathbf{G}_1 + \Theta_1\mathbf{G}_{\tau 1} + \mathbf{R}_1 = A_2\mathbf{w}_2 + Q_2\mathbf{G}_2 + \Theta_2\mathbf{G}_{\tau 2} + \mathbf{R}_2, \tag{20}$$

where

$$A_i = \begin{bmatrix} & B_i\mathbf{n} \\ (B_i\mathbf{n})^T & \end{bmatrix}, \qquad Q_i = \begin{bmatrix} -T_i & \\ & -\frac{\lambda_i}{\mu}\Delta t \end{bmatrix} + r_i A_i, \tag{21}$$

$$\Theta_i = \begin{bmatrix} -\Gamma_i & \\ & -\frac{\gamma_i^T}{\mu}\nabla t \end{bmatrix} + A_i[I \otimes \pm(\mathbf{x}_\delta - \mathbf{y}_i)^T], \qquad \mathbf{R}_i = \left[\frac{\nabla t}{\mu}\rho g \nabla z \cdot K_i\mathbf{n} - \mathbf{u}\frac{0}{\delta i}\cdot B_i\mathbf{n}\right], \tag{22}$$

and where A_i and Q_i are 4 × 4 matrices, Θ_i is a 4 × 12 matrix and $\mathbf{R}_i$ is a 4 × 1 vector.

According to equation (13) the tangential projections of the gradients are $\mathrm{G}_{\tau 1} = \mathbf{G}_{\tau 2} = \mathbf{G}_\tau$. Deriving $\mathbf{G}_2$ from equation (13) and substituting the result into equation (20) we obtain the following expression for $\mathbf{G}_1$

$$(r_1Q_2 + r_2Q_1)\mathbf{G}_1 = (r_2A_2 + Q_2)\mathbf{w}_2 - (r_2A_2 + Q_2)\mathbf{w}_1 + \left(Q_2[I \otimes (\mathbf{y}_1 - \mathbf{y}_2)^T] + r_2(\Theta_2 - \Theta_1)\right)\mathbf{G}_\tau + r_2(\mathbf{R}_2 - \mathbf{R}_1). \tag{23}$$

Substituting equation (23) into the left-hand side of equation (20), one obtains the following multi-point approximation for the traction $\mathbf{F}$, as given in equation (7), and the total fluid flux $q_t = q + (\tilde{q}^{n+1} - \tilde{q}^n)/\Delta t$:

$$\begin{aligned} [\mathbf{F}_{qt\nabla t}] = {} & Q_1\left(r_1Q_2 + r_2Q_1\right)^{-1}Q_2(\mathbf{w}_2 - \mathbf{w}_1 + [I \otimes (\mathbf{y}_1 - \mathbf{y}_2)^T]\mathbf{G}_\tau) + \\ & + r_1Q_2\left(r_1Q_{2+}r_2Q_1\right)^{-1}(A_1\mathbf{w}_1 + \Theta_1\mathbf{G}\tau + \mathbf{R}_1) + r_2Q_1\left(r_1Q_{2+}r_2Q_1\right)^{-1}(A_2\mathbf{w}_2 + \Theta_2\mathbf{G}\tau + \mathbf{R}_2). \end{aligned} \tag{24}$$

The coupled multi-point approximation (24) was presented in Terekhov (2020a). Approximation of boundary conditions (10) requires a specific treatment and we refer to Terekhov (2020a) for the details. The approximation (24) involves fluid properties which may depend on pore pressure or composition in the case of multicomponent flow. In such cases equation (24) can not be applied directly and further steps are required, as will be discussed below.

Gradient Reconstruction

The approximation (24) requires the the tangential projection of the gradients of the unknowns to be reconstructed. One can derive $\mathbf{G}_2$ from equation (20) and substitute it into equation (13) to obtain the following interpolation equation

$$\left(Q_2[I\otimes(\mathbf{x}_2-\mathbf{x}_1)^T+r_2(Q_1-Q_2)[I\otimes\mathbf{n}^T]+r_2(\Theta_1-\Theta_2)\right)[\nabla\otimes\mathbf{w}_1]= \\ =(Q_2+r_2A_2)\mathbf{w}_2-(Q_2+r_2A_1)\mathbf{w}_1+r_2(\mathbf{R}_2-\mathbf{R}_1). \tag{25}$$

It is necessary to consider at least 3 interfaces (in 3D) of the first cell to enclose the system with respect to the 12 components of $\nabla\otimes\mathbf{w}_1$.

Bringing together the results of equation (25) for N considered interfaces of the ith cell, we build up the system

$$M_i(\nabla\otimes\mathbf{W}_i)=D_iU_i, \tag{26}$$

where M_i is a $4N\times 12$ matrix and D_i a $4N\times 4(N+1)$ matrix of unit matrices $\{I, -I\}$ in front of the corresponding unknowns at the right-hand side of equation (25), while U_i is a $4(N+1)\times 1$ vector of $N+1$ displacements (or boundary conditions). The solution of equation (26) can be obtained in a least-squares sense according to

$$\nabla\otimes\mathbf{W}_i=\left(M_i^TM_i\right)^{-1}M_i^TD_iU_i. \tag{27}$$

For the approximation of $\mathbf{G}_\tau$ in equation (24) the following combination of gradients is used in Terekhov (2020a)

$$\mathbf{G}_\tau=\frac{\mathbf{G}_{\tau 1}+\mathbf{G}_{\tau 2}}{2}. \tag{28}$$

A set of cells that contribute to the approximation (28) for each interface of some cell i is illustrated in Fig. 1.

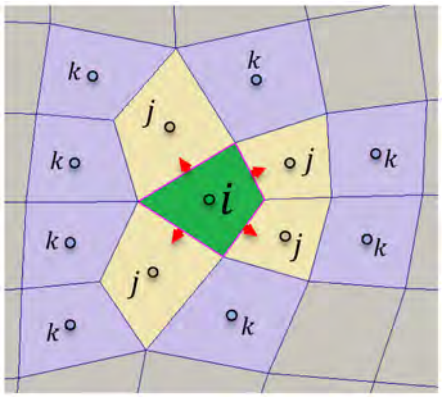

Figure 1—Cells that contribute to the approximation of fluxes over the interfaces of cell *i*. Index *j* denotes the the close neighbours of cell *i*. Index *k* denotes further neighbours that contribute to the gradients reconstructed in cells *j*.

Introducing Discontinuity

Displacements can be discontinuous at faults. In that case equation (13) does not hold anymore and the tangential gradients of the displacements may be different at different sides of the fault. We introduce an additional degree of freedom (d.o.f.) per faulted interface, namely-gap vector $\mathbf{g}\equiv\{\mathbf{g}, 0\}=\mathbf{w}_2^+-\mathbf{w}_1^-$ which is equal to the jump of displacements over the interface and remains zero for the jump of pressure. The following continuity condition will be used instead of equation (13)

$$\mathbf{w}_1 \pm g + [I \bigotimes (\mathbf{x}_\delta - \mathbf{x}_1)^T](\nabla \bigotimes \mathbf{w}_1) = \mathbf{w}_2 + [I \bigotimes (\mathbf{x}_\delta - \mathbf{x}_2)^T](\nabla \bigotimes \mathbf{w}_2), \tag{29}$$

where "±" is positive when the first and second cells are located at negative and positive sides of the fault respectively. The continuity of fluxes, as given in equation (20), can be rewritten as

$$A_1\mathbf{w}_1 \pm A_1 g + Q_1\mathbf{G}_1 + \Theta_1\mathbf{G}_{\tau 1} + \mathbf{R}_1 = A_2\mathbf{w}_2 + Q_2\mathbf{G}_2 + \Theta_2\mathbf{G}_{\tau 2} + \mathbf{R}_2, \tag{30}$$

expression (23) changes to

$$\begin{aligned}(r_2Q_1 + r_1Q_2)\mathbf{G}_1 = (Q_2 + r_2A_2)\mathbf{w}_2 - (Q_2 + r_2A_1)\mathbf{w}_1 \mp (Q_2 + r_2A_1)g + \\ + \left(r_2\Theta_2 + Q_2[I \bigotimes (\mathbf{x}_\delta - \mathbf{y}_2)^T]\right)\mathbf{G}_{\tau 2} - \left(r_2\Theta_1 + Q_2[I \bigotimes (\mathbf{x}_\delta - \mathbf{y}_1)^T]\right)\mathbf{G}_{\tau 2} + r_2(\mathbf{R}_2 - \mathbf{R}_1),\end{aligned} \tag{31}$$

equation (24) becomes

$$\begin{aligned}\begin{pmatrix}\mathbf{F} \\ q_t\nabla t\end{pmatrix} = Q_1\left(r_1Q_2 + r_2Q_1\right)^{-1}Q_2(\mathbf{w}_2 - \mathbf{w}_1 \mp g + [I \bigotimes (\mathbf{y}_1 - \mathbf{y}_2)^T]\mathbf{G}_{\tau 1}) + \\ + r_1Q_2\left(r_1Q_2 + r_2Q_1\right)^{-1}(A_1\mathbf{w}_1 \pm A_1 g + \Theta_1\mathbf{G}_{\tau 1} + \mathbf{R}_1) + \\ + r_1Q_2\left(r_1Q_2 + r_2Q_1\right)^{-1}(A_2\mathbf{w}_2 + \Theta_2\mathbf{G}_{\tau 1} + \mathbf{R}_2) \pm \\ \pm (Q_1(r_1Q_2 + r_2Q_1)^{-1}Q_2[I \bigotimes (\mathbf{x}_\delta - \mathbf{y}_2)^T + r_2Q_1(r_1Q_2 + r_2Q_1)^{-1}\Theta_2)(\nabla \bigotimes g).\end{aligned} \tag{32}$$

Also, the following expression can be used for gradient reconstruction instead of equation (25)

$$\begin{aligned}\left(Q_2[I \bigotimes (\mathbf{x}_2 - \mathbf{x}_1)^T] + r_2(Q_1 - Q_2[I \bigotimes \mathbf{n}^T] + r_2(\Theta_1 - \Theta_2)\right)[\nabla \bigotimes \mathbf{w}_1] = \\ = (Q_2 + r_2A_2)\mathbf{w}_2 - (Q_2 + r_2A_1)\mathbf{w}_1 \mp (Q_2 + r_2A_1)g + r_2(\mathbf{R}_2 - \mathbf{R}_1 0 \mp \\ \mp (Q_2[I \bigotimes (\mathbf{y}_2 - \mathbf{x}_\delta)] - r_2\Theta_2)[\nabla \bigotimes g]\end{aligned} \tag{33}$$

where gap gradients are reconstructed by simply using

$$I \bigotimes (\mathbf{x}_2 - \mathbf{x}_1)^T(\nabla \bigotimes g_1) = g_2 - g_1. \tag{34}$$

The approximation of the traction, as given in equation (32), remains correct while $\mathbf{n}_\Gamma\mathbf{g} = 0$. When $\pm\mathbf{n}_\Gamma\mathbf{g} > 0$ the traction should be set to zero, $\mathbf{F} = \mathbf{0}$, which corresponds to a free boundary condition.

We use a Discrete Fracture Model (DFM) approach for the flow which implies having discrete equations for fracture segments of non-zero volume. We assume continuous pressure in equation (13), and we have two matrix-fracture connections per fracture segment in the fluid mass balance for that segment. For the fluid fluxes between fracture segments we use a two-point flux approximation (TPFA).

Reconstruction of Stresses

Solving the system of discrete equations (12) provides the vector of unknowns in the cell centers. To reconstruct effective stresses at the same locations we use the algorithm described in Terekhov (2020a).

For the jth interface of the cell let us construct the following matrices:

$$\mathcal{N}_i = \begin{pmatrix} n_x & 0 & 0 & 0 & n_z & n_y \\ 0 & n_y & 0 & n_z & 0 & n_x \\ 0 & 0 & n_z & n_y & n_x & 0 \end{pmatrix}, \mathcal{T}_j = \begin{pmatrix} x_j - x_V & 0 & 0 & 0 & \frac{z_j - z_V}{2} & \frac{y_j - y_V}{2} \\ 0 & y_j - y_V & 0 & \frac{z_j - z_V}{2} & 0 & \frac{x_j - x_V}{2} \\ 0 & 0 & z_j - z_V & \frac{y_j - y_V}{2} & \frac{x_j - x_V}{2} & 0 \end{pmatrix}, \tag{35}$$

where n_x, n_y and n_z are components of the unit normal to the jth interface; x_j, y_j and z_j are components of the jth interface center position; and x_V, y_V and z_V are components of the cell center position.

Collecting these matrices for N interfaces of the cell we will obtain the following $3N \times 6$ and $3N \times 6$ matrices, and $3N \times 1$ vector

$$\mathcal{N} = \begin{pmatrix} \delta_1 \mathcal{N}_1 \\ \cdots \\ \delta_N \mathcal{N}_N \end{pmatrix}, \boldsymbol{\gamma} = \begin{pmatrix} \boldsymbol{\gamma}_1 \\ \cdots \\ \boldsymbol{\gamma}_N \end{pmatrix}, F' = \begin{pmatrix} \delta_1(\mathrm{F}_1 + \mathrm{b}_{P\delta 1}) \\ \cdots \\ \delta_N(\mathrm{F}_N + \mathrm{b}_{P\delta N}) \end{pmatrix}, \tag{36}$$

where vector **b** represents the tensor of Biot's coefficients B in Voigt notation: $\mathbf{b} = \{b,b,b,0,0,0\}_T$. The stresses at the cell center can then be reconstructed using the least squares solution

$$\boldsymbol{\sigma}' = (\boldsymbol{\gamma}^T \mathcal{N})^{-1} \boldsymbol{\gamma}^T F, \tag{37}$$

where the effective stress tensor $\boldsymbol{\sigma}' = \{\sigma'_{xx}, \sigma'_{yy}, \sigma'_{zz}, \sigma'_{yz}, \sigma'_{xz}, \sigma'_{xy}\}^T$ is written in Voigt notation.

Solution Strategy

Discretization

In real-world subsurface applications the fluid is usually represented as a mixture composed of multiple chemical components and phases. In the case of multiphase multicomponent fluid flow its quantities like density, viscosity and others depend on mole fractions, pressure and temperature. Equations (32) and (33) involve fluid viscosity and density (in the gravity term) which means that they may depend at least on pressure. These approximations become non-resolved with respect to pressures. It is therefore required to repeat the gradient reconstruction and the approximations each nonlinear iteration.

Assuming that the tensor of Biot coefficients remains constant, the terms that include Biot coefficients can be omitted in the local problem for poromechanics. This allows fluid density and viscosity to be excluded from these expressions and approximations (32) to be calculated once before iterations over time. Density and viscosity can be taken into account having the equations for fluid flow (8) and flux of displacement (9) already approximated.

This requires separate assembly of Darcy, Biot and gravity terms in equation (8). The Biot term does not affect the reconstruction of the gradients beacuse the tensor of Biot coefficients is constant over the domain whereas the gradients are linear with respect to the gravity contribution. In turn, approximations of tractions and the terms in the fluid flow expression are linear with respect to gradients and gravity. This operation can be performed by omitting all left-bottom terms in matrices (21) and (22) and the Biot terms in vectors $\mathbf{R}_1$ and $\mathbf{R}_2$ and setting $\Delta t = 1$ in the other terms. This technique, as introduced in Terekhov (2020a), allows us to retrieve the approximation of the Darcy flux q separately from the Biot contribution $(\tilde{q}^{n+1} - \tilde{q}^n)/\Delta t$, and to decouple fluid properties from approximation of fluxes. It also allows us to calculate the coefficients of the approximations at the pre-processing stage. The flux of displacement $\tilde{q}$ can then be calculated as follows:

$$\begin{aligned} \tilde{q} = r_1 \tilde{A}_1 \left(r_2 Q_1 + r_1 Q_2 \right)^{-1} (Q_2 + r_2 A_2) \mathbf{w}_2 - (r_1 \tilde{A}_1 (r_2 Q_1 + r_1 Q_2)^{-1} (Q_2 + r_2 A_2) - \tilde{A}_1)(\mathbf{w}_1 \pm g) + \\ + r_1 \tilde{A}_1 \left(r_2 Q_2 + r_1 Q_2 \right)^{-1} (r_2 \Theta_2 + Q_2 [I \otimes (\mathbf{x}_\delta - \mathbf{y}_2)^T]) \mathbf{G}_{\tau 2} - \\ - (r_1 \tilde{A}_1 (r_2 Q_1 + r_1 Q_2)^{-1} (r_2 \Theta_2 + Q_2 [I \otimes (\mathbf{x}_\delta - \mathbf{y}_2)^T]) - \tilde{A}_1 [I \otimes (\mathbf{x}_\delta - \mathbf{y}_1)]) \mathbf{G}_{\tau 1} + \\ + r_1 \tilde{A} \left(r_2 Q_1 + r_1 Q_2 \right)^{-1} r_2 (\mathbf{R}_2 - \mathbf{R}_1), \end{aligned} \tag{38}$$

where $\tilde{A}_1$ is equal to

$$\tilde{A}_1 = \begin{pmatrix} 0 \\ (B_1 \mathbf{n})^T \end{pmatrix}. \tag{39}$$

At the boundaries this flux can be calculated separately as well; see Terekhov (2020a).

The first stage of discretization consists of the reconstruction of gradients according to equations (25), (33) and (34). We note that the least squares approach used in equation (27) can results in negative-valued

coefficients in front of the terms $\mathbf{w}_2 - \mathbf{w}_1$ and $\mathbf{w}_1 - \mathbf{w}_2$ in the first and second cells respectively. This may lead to monotonicity issues and oscillating solutions which are common problems in multi-point approximations.

Once the gradients are reconstructed they can be used to approximate fluxes according to equations (24), (32) and (38). For non-faulted interfaces the averaged gradient as defined in equation (28) is used.

Linear Solvers

In order to improve the efficiency of the solution of the system of equations (1), an advanced linear solver strategy is required. In White et al. (2016), a fixed-stress split concept is used to construct a block-partitioned preconditioner for poromechanics, which was extended for coupled multiphase flow and mechanics in Klevtsov et al. (2016). Here we employ the first stage of this approach to construct a preconditioner.

The idea of the method is to consider the following block-partitioned linear system:

$$L^{-1}J\delta\mathbf{w} = \begin{pmatrix} I & 0 \\ -J_{Pu}J_{uu}^{-1} & I \end{pmatrix}\begin{pmatrix} J_{uu} & J_{up} \\ J_{pu} & J_{pp} \end{pmatrix}\begin{pmatrix} \delta\mathbf{u} \\ \delta\mathbf{P} \end{pmatrix} = \begin{pmatrix} J_{uu} & J_{up} \\ 0 & S_{pp} \end{pmatrix}\begin{pmatrix} \delta\mathbf{u} \\ \delta\mathbf{P} \end{pmatrix} = -\begin{pmatrix} \mathrm{r}_{\mathbf{u}} \\ \mathrm{r}_{\mathbf{P}} - J_{pu}J_{uu}^{-1}\mathrm{r}_{\mathbf{u}} \end{pmatrix}, \tag{40}$$

where J, $\mathbf{r_u}$ and $\mathbf{r_p}$ are the Jacobian and the residuals for momentum and mass balance equations produced by the numerical scheme, $\delta\mathbf{u}$ and $\delta\mathbf{p}$ are unknown increments of the vector of displacements and pressure, J_{uu},J_{up},J_{pu},J_{pp} are contributions to momentum balance and mass balance equations from displacement and pressure unknowns, L is the lower-triangular term in an LDU decomposition of the Jacobian, and $S_{pp} = J_{pp} - J_{pu}J_{uu}^{-1}J_{up}$ represents the Schur complement of block J_{uu} in the Jacobian.

The concept of fixed-stress splitting is used here to provide the following sparse approximation of S_{pp}

$$\tilde{S}_{pp} = J_{pp} - \mathrm{diag}\left(J_{pu}P_u^{-1}J_{up}\cdot \mathrm{e}\right), \tag{41}$$

where $\mathbf{e} = [1, 1, .., 1]_T$ is a probing vector, and P_u^{-1} is a preconditioner used for the elasticity system.

This preconditioner is applied as follows. At the begining of every nonlinear (Newton) iteration, $\tilde{S}_{pp}$ is evaluated. A single V-cycle of an algebraic multi-grid (AMG) solver is typically used for P_u^{-1}. Next, the solution of upper triangular system (40) is approximated every iteration of the linear solver and provided to it as an initial guess. The system for the pressure unknowns is preconditioned using a single V-cycle as well. The generalized minimal residual (GMRES) method is used as an outer solver.

Elasticity Test Cases

Convergence Study

We made comparison with analytical solution proposed in Terekhov and Tchelepi (2020) to check the order of approximation on different grids. We consider a 3D unit cubic domain $\Omega = [0,1]^3$ and assume that the following reference solution holds in the domain

$$u_x = (x-0.5)^2 - y - z, \quad u_y = (y-0.5)^2 - x - z, \quad u_z = (z-0.5)^2 - x - y.$$

As a stiffness matrix we consider the following matrix

$$C = \begin{bmatrix} 1.323 & 0.0726 & 0.263 & 0.108 & -0.08 & -0.239 \\ 0.0726 & 1.276 & -0.318 & 0.383 & 0.108 & 0.501 \\ 0.263 & -0.318 & 0.943 & -0.183 & 0.146 & 0.182 \\ 0.108 & 0.383 & -0.183 & 1.517 & -0.0127 & -0.304 \\ -0.08 & 0.108 & 0.146 & -0.0127 & 1.209 & -0.326 \\ -0.239 & 0.501 & 0.182 & -0.304 & -0.326 & 1.373 \end{bmatrix}. \tag{42}$$

To satisfy the momentum balance in equation (1) we have to put $\mathbf{f} = -\nabla\cdot\sigma = 2\{c_{11} + c_{26} + c_{35}, c_{16} + c_{22} + c_{34}, c_{15} + c_{24} + c_{33}\}$ at the right side inside the domain and apply Dirichlet boundary conditions according to the reference solution.

To assess the convergence of the numerical solutions we calculate the discrete L_2 norm of their deviation from the reference solution. Results are presented in Table 1 for calculations performed using a structured cubic mesh, an unstructured mesh of wedges and an unstructured hexahedral mesh. The last two meshes are extruded along the z-axis and are truly unstructured only in the x-y plane. The solution obtained on the structured cubic mesh demonstrates 2nd-order of convergence with respect to displacements and more than 1st-order convergence with respect to stresses. On the unstructured wedge mesh the solution also shows 2nd-order convergence with respect to displacements and nearly 1st-order convergence with respect to stresses.

Table 1—L_2 norms of errors computed on structured cubic, unstructured extruded wedge and unstructured extruded hexahedral meshes.

cubic mesh			wedge mesh			hexahedral mesh		
N. of cells	$\|\|\mathbf{u} - \mathbf{u}_h\|\|L_2$	$\|\|\sigma - \sigma_h\|\|L_2$	**N.** of cells	$\|\|\mathbf{u} - \mathbf{u}_h\|\|L_2$	$\|\|\sigma - \sigma_h\|\|L_2$	**N.** of cells	$\|\|\mathbf{u} - \mathbf{u}_h\|\|L_2$	$\|\|\sigma - \sigma_h\|\|L_2$
27	1.89E-2	1.93E-1	168	6.58E-3	1.56E-1	84	1.08E-2	1.41E-1
125	7.1E-3	9.11E-2	340	4.18E-3	1.16E-1	225	5.98E-3	8.42E-2
1000	1.86E-3	3.08E-2	2440	1.17E-3	5.24E-2	1190	1.94E-3	3.72E-2
2744	9.62E-4	1.81E-2	18920	3.04E-4	2.34E-2	9280	5E-4	1.44E-2
8000	4.76E-4	1.02E-2	-	-	-	-	-	-
order	1.975	1.6	order	1.943	1.16	order	1.957	1.37

Displaced Fault

Faulted reservoirs can undergo different mechanical conditions over their geological history. Nearly always this results in an offset such that stratigraphic layers become displaced.

An analytical investigation of stresses initiated around a displaced fault in a depleted reservoir was carried out in Jansen et al. (2019). Here we compare the solution we obtained numerically with the analytical one. The model domain is illustrated in Fig. 2a. It consists of three regions which are treated as elastic bodies with shear modulus $G = 6.5$ GPa and Poisson's coefficient $\nu = 0.15$. Only the reservoir (in the middle) admits a non-zero pore pressure with Biot's coefficient $\alpha = 0.9$.

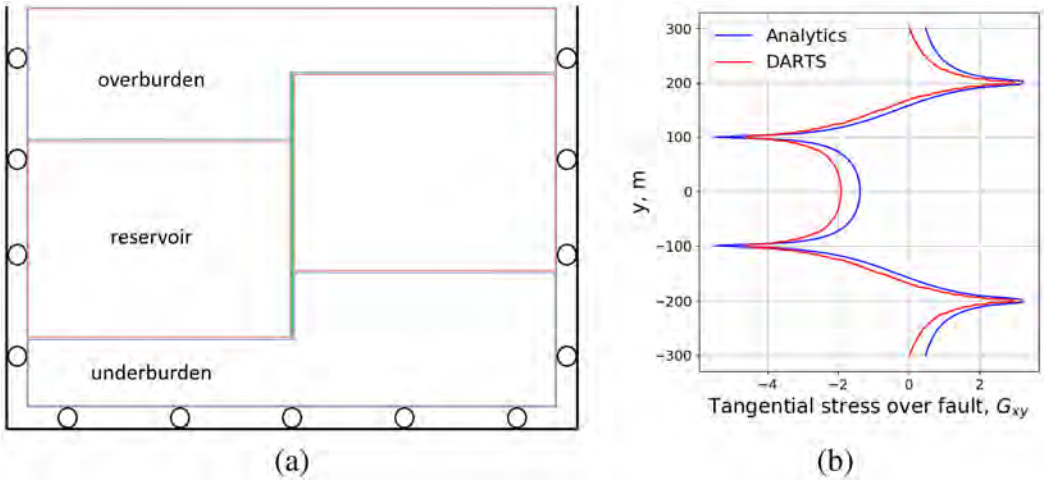

Figure 2—The domain with a vertical displaced fault and boundary conditions (a). Only inside the reservoir, the pore pressure was subtracted from the stress tensor. Tangential stress profile over the vertical centerline calculated using analytics and numerical simulation (b).

Comparisons of the numerical solutions with the analytical is displayed in Fig. 2b. A build-up of pore pressure by $\Delta p = 20$ MPa inside the reservoir (width 800 m, height 300 m and offset 100 m) perturbs the

system. The calculated profile of the shear component of the stress tensor over the vertical centerline of the domain is compared against the analytical result. There is a small discrepancy between the numerical and analytical solution which can be explained by the influence of boundary conditions in numerical calculations: the numerical simulation is made for a finite-width reservoir, whereas the analytical solution assumes an infinite width.

Contact Problem

The next case concerns a fault with Coulomb friction in the center of a square domain of size a; see Fig. 3. The right boundary is fixed, the top and bottom boundaries are free of any forces, while displacements $u_{left} = \{0.001, 0.01\}$ are prescribed at the left. A plane strain setup is considered. The stiffness matrix is determined by Lam´e coefficients $\lambda = G = 1$. A fault of length $L = 0.4a$ with friction coefficient $\eta = 0.85$ is allowed to slip once the Coulomb criterion (11) is exceeded and the fault is prohibited from opening. A structured quadrilateral grid is used in in the calculation. The resulting displacement and stress fields for the verical fault are shown in Figs. 4 and 5. One can notice the small jump in horizontal displacements at the fault.

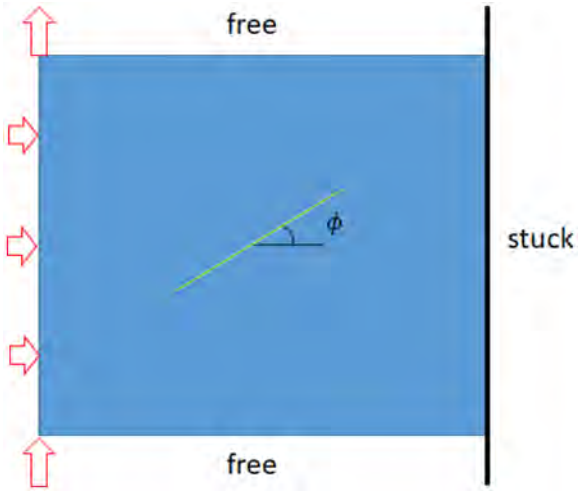

Figure 3—The domain with an inclined fault and boundary conditions.

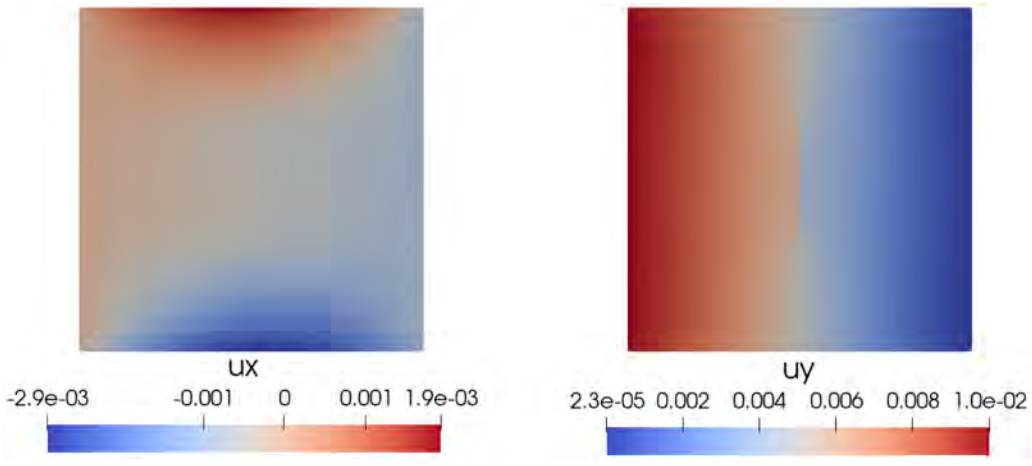

Figure 4—Horizontal (left) and vertical (right) displacements for the case of a vertical fault (φ = 90₀). Note the jump in vertical displacements at the fault.

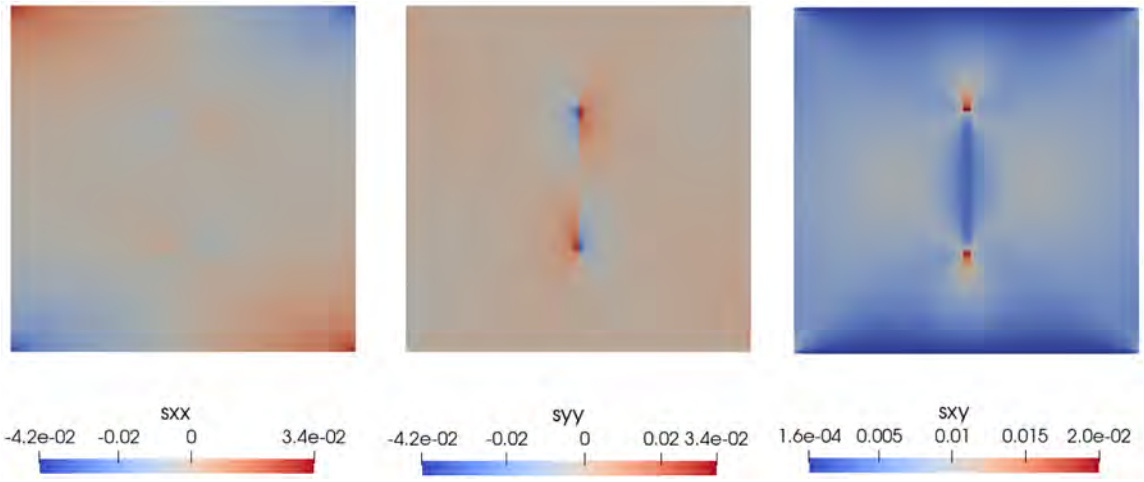

Figure 5—Normal horizontal (left), vertical (middle) and shear stresses (right) for the case of a vertical fault ($\varphi = 90_o$).

The results are compared with other ones, obtained by the PorePy simulation tool (Keilegavlen et al., 2021), for different orientations of the fault determined by a dip angle φ. The comparison is displayed in Fig. 6. Tangential tractions over the fault calculated by DARTS and PorePy match quite well. For higher dip angles (nearly vertical orientation) the resulting slip also fits quite well. However, for lower dip angles the slip is decreasing and in the case of $\varphi = 72_o$ it becomes located at the tips of the fault whereas the center of the fault displays higher normal tractions and smaller slip values. With decreasing dip angles, the slip magnitude decreases as well and a tiny mismatch in tangential traction results in a higher mismatch in slip (for $\varphi = 72_o$). Below some threshold angle no slip over the fault is observed.

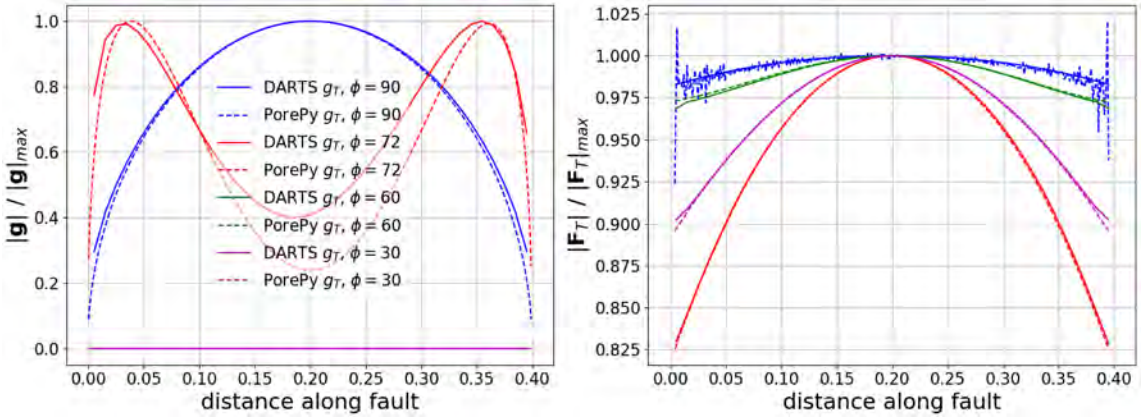

Figure 6—Comparison of slip and tangential traction along the fault for different dip angles.

Oscillations

The figures displayed in the previous subsection were calculated using structured rectangular grid which provided stable solution. However, attempt to calculate contact problem using unstructured wedge grid resulted in noisy slip curve along the fault. The reason is oscillated (normal and tangential) tractions provided by the scheme even for completely continuous displacements (zero slip).

Traction over the fault for the setup described in the previous paragraph but with $\eta = 3.2$ is illustrated in Fig. 7 where it is presented by the magnitude of harmonic

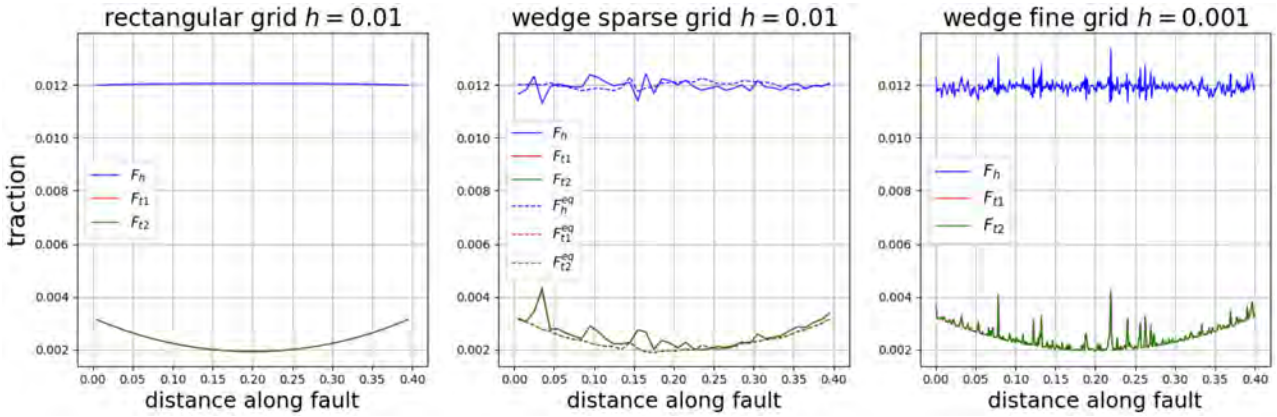

Figure 7—Traction along the fault represented by the magnitude of harmonic F_h and transversal F_{ti} terms for the setup from the previous paragraph with φ = 90$_o$ calculated using different grids: a structured rectangular grid and an unstructured wedge-type grid (extruded along the z-axis). F_h – harmonic term, F_{ti} – transversal terms. Note the oscillatory tangential and normal traction along the contact. Mesh refinement does not decrease the magnitude of oscillations whereas a grid composed of wedges of the same size as the rectangles results in less noisy profiles.

$$\mathbf{F}_h = T(\mathbf{u}_1 - \mathbf{u}_2) \tag{43}$$

and transversal

$$\mathbf{F}_{ti} = -\left(T\left[I \bigotimes (\mathbf{y}_1 - \mathbf{y}_2)^T\right] + r_1 T_2 (r_1 T_2 + r_2 T_1)^{-1} \Gamma_1 + r_2 T_1 (r_1 T_2 + r_2 T_1)^{-1} \Gamma_2\right)[\nabla \bigotimes \mathbf{u}_i] \tag{44}$$

terms where $T = T_1(r_1T_2 + r_2T_1)^{-1}T_2$. These terms represent contributions to the total traction in (24), where the harmonic one is proportional to $\mathbf{w}_2 - \mathbf{w}_1$ in the first term in (24) and the transversal one is proportional to $\mathbf{G}_\tau$ taken from all terms in (24). The gap vector at the contact is zero. This value of friction coefficient is chosen to consider more challenging case when only the part of the fault exhibits slip whereas another part remains stuck. Cases using a rectangular grid, a wedge-type sparse grid with increased resolution h = 0.01 near the fault, a wedge-type sparse grid with equal element size h = 0.01 and a fine wedge-type grid with h = 0.001 are considered. See Fig. 8 in which the corresponding slip profiles and the magnitudes of the tangential traction F_T have been displayed.

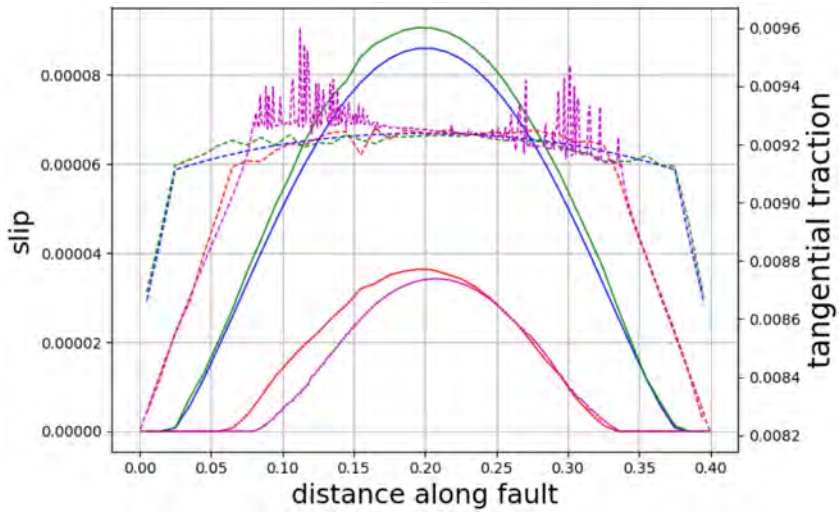

Figure 8—Slip (solid lines) and effective tangential traction F_T (dashed lines) along the fault calculated using a rectangular grid (blue), a wedge-type sparse grid with h = 0.01 (red), a wedge-type sparse grid of equally sized elements with h = 0.01 (green), and a wedge-type fine grid with h = 0.001 (magenta).

The solution obtained using a rectangular grid demonstrates smooth profiles of slip and traction along the fault and is therefore considered to be the correct one. Although the solution obtained using the wedge-type grid with the same element size $h = 0.01$ exhibits oscillations, the resulting profiles of slip and traction provide a good match with the correct solution. The profiles calculated using wedge-type grids with different resolutions (both the coarse grid with $h = 0.01$ and the fine one with $h = 0.001$ have element size $h = 0.1$ near the boundary of the domain) exhibit oscillations which remain the same or even increase in magnitude for grids with higher resolutions. As a result, slip profiles obtained with these grids are of a significantly lower quality than the correct one.

The unstable solution associated with oscillations in the slip and traction profiles results from the use of a multi-point stress approximation (MPSA) and can be caused by the violation of the coercivity condition (Keilegavlen and Nordbotten, 2017). The authors proposed a modified MPSA that weakly imposes the symmetry of the stress tensor -a concept originally used to obtain hybrid mixed finite element formulations (Arnold et al., 2007).

Poromechanics test cases

Linearity Preservation

Consider a cubic domain $\Omega = [0,1]^3$ of a poroelastic body with the following constant stiffness matrix, Biot and permeability tensors (Terekhov, 2020a):

$$C = \begin{bmatrix} 93 & 46 & 22 & 13 & 72 & 35 \\ 46 & 95 & 41 & 62 & 56 & 24 \\ 22 & 41 & 89 & 25 & 33 & 21 \\ 13 & 62 & 25 & 87 & 13 & 25 \\ 72 & 56 & 33 & 13 & 99 & 57 \\ 35 & 24 & 21 & 25 & 57 & 78 \end{bmatrix}, \quad B = \begin{bmatrix} 1 & 6 & 5 \\ 6 & 67 & 27 \\ 5 & 27 & 76 \end{bmatrix}, \quad K = \begin{bmatrix} 25 & 2 & 39 \\ 2 & 42 & 7 \\ 37 & 7 & 100 \end{bmatrix}, \tag{45}$$

with the following linear reference solution:

$$\begin{bmatrix} u \\ v \\ w \\ p \end{bmatrix} = \begin{bmatrix} 1 & 2 & 3 & 4 \\ 6 & 7 & 8 & 9 \\ 11 & 12 & 13 & 14 \\ 16 & 17 & 18 & 19 \end{bmatrix} \begin{bmatrix} x \\ y \\ z \\ t \end{bmatrix} + \begin{bmatrix} 5 \\ 10 \\ 15 \\ 20 \end{bmatrix}, \tag{46}$$

which satisfies the system equations (1). Note that in this example we employ a full Biot matrix B. Although such a matrix is of no physical significance for practical applications it serves to test computational aspects of the algorithm. We assume density and viscosity in (6) remain constant and porosity is equal to

$$\phi = \frac{p - p^0}{M} + \nabla \cdot B(\mathbf{u} - \mathbf{u}^0), \tag{47}$$

where M is Biot's modulus, p,^{0} $\mathbf{u}^0$ are fluid pressure and displacement vector at reference state. Substituting equations (46), (45) and (47) into equation (1) we can derive the right-hand side terms. Using these, while specifying initial and boundary (Dirichlet) conditions according to equation (46), we expect to observe this reference solution inside the cube. The parameteres that make sense for calculation are listed in Tab. 2.

Table 2—Parameters used for calculations in linearity preservation test case.

μ, cP	g, bar·m^2/kg	1/M, bar^{-1}	ρf, kg/m^3
9.81E-2	0	1.45E-06	978

The results are summarized in Table 3. The calculations were performed using structured grids composed of cubes and wedges, and an unstructured tetrahedral grid up to time $T = 1$. The linear solution was observed

for every time step and for each type of grid. Absolute errors at $t = T$ with respect to the reference solution (46) are almost at the level of machine double floating-point precision.

Table 3—Absolute errors of solutions calculated on different mesh types for Test Case 1.

Cell geometry	Nr. of cells	$\|\|\mathbf{u} - \mathbf{u}_h\|\|L_2$	$\|\|p - p_h\|\|_{L2}$,
Cubic	64	3.0E-12	7.99E-11
Cubic	8000	3.38E-12	7.29E-10
Wedge	16000	7.14E-14	2.53E-11
Tetrahedron	16030	1.82E-11	4.55E-12

Convergence

For the same $\Omega = [0,1]^3$ cubic domain consider the following constant stiffness matrix, and Biot and permeability tensors:

$$C = \begin{bmatrix} 1.323 & 0.0726 & 0.263 & 0.108 & -0.08 & -0.239 \\ 0.0726 & 1.276 & -0.318 & 0.383 & 0.108 & 0.501 \\ 0.263 & -0.318 & 0.943 & -0.183 & 0.146 & 0.182 \\ 0.108 & 0.383 & -0.183 & 1.517 & -0.0127 & -0.304 \\ -0.08 & 0.108 & 0.146 & -0.0127 & 1.209 & -0.326 \\ -0.239 & 0.501 & 0.182 & -0.304 & -0.326 & 1.373 \end{bmatrix}, B = \begin{bmatrix} 1.5 & 0.5 & 0.5 \\ 0.1 & 1.5 & 0.15 \\ 0.5 & 0.15 & 1.5 \end{bmatrix}, K = \begin{bmatrix} 1.5 & 0.5 & 0.35 \\ 0.5 & 1.5 & 0.45 \\ 0.35 & 0.45 & 1.5 \end{bmatrix}, \tag{48}$$

and the following reference solution (Terekhov, 2020a):

$$\begin{aligned} u(x, y, z, t) &= \left[(x-0.5)^2 - y - z\right](1+t^2) \\ u(x, y, z, t) &= \left[(x-0.5)^2 - x - z\right](1+t^2) \\ u(x, y, z, t) &= \left[(x-0.5)^2 - x - y\right](1+t^2) \\ p(x, y, z, t) &= \frac{1}{2\sin(1)}\sin\left((1-x)(1-y)(1-z)\right) + 0.5(1-x)^3(1-y)^2(1-z)(1+t^2). \end{aligned} \tag{49}$$

The source terms $\mathbf{f}$ and f are calculated by substituting equation (48), (47) and (49) into equation (1) using automatic differentiation. Dirichlet boundary and initial conditions are applied according to equation (49). We assume density and viscosity in (6) remain constant and porosity is calculated according (47). All relevant parameters used in the calculations are listed in Table 4.

Table 4—Parameters used for calculations in convergence test case.

μ, cP	g, bar·m²/kg	$1/M$, bar^{-1}	ρ_f, kg/m³
9.81E-2	-9.81E-2	1.45E-06	978

Table 5—Absolute errors of solutions calculated on a cubic mesh for convergence test case.

Cell geometry	Nr. of cells	Δt	$\|\|\mathbf{u} - \mathbf{u}_h\|\|_{L2}$	$\|\|p - p_h\|\|_{L2}$,
Cubic	64	0.1	1.16E-2	4.9E-2
Cubic	512	0.5	3E-3	1.13E-2
Cubic	4096	0.25	9.15E-4	5.14E-3
Cubic	32768	0.125	3E-4	2.48E-3
	convergence order		1.6	1.05

Mandel Problem

Consider a rectangular domain illustrated in Fig. 9. Roller boundary conditions are applied to the left and bottom boundaries of the domain. The right boundary is free of both normal and tangential forces whiles

a normal load is applied from the top. No-flow conditions are specified for all boundaries except for the right one where a Dirichlet condition $p = p_0$ is applied. This set-up is the so-called Mandel problem which is often used as an example to demonstrate specific aspects of poroelasticity (Coussy, 2003).

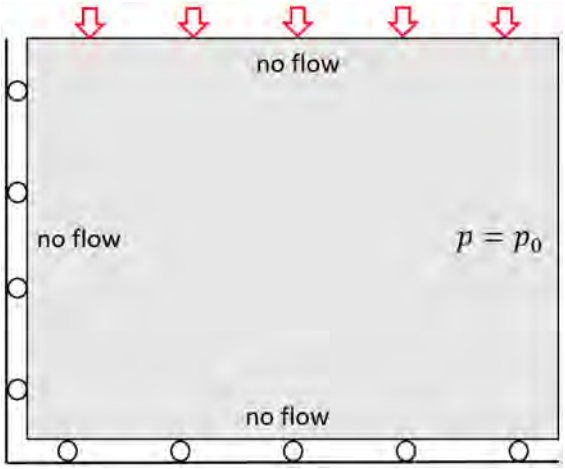

Figure 9—The domain and boundary conditions for Mandel problem.

We consider a porous homogeneous domain characterized by Young's modulus $E = 1$GPa, Poisson's ratio $\nu = 0.25$, a diagonal permeability tensor $k_x = k_y = k_z = 1$mD, saturated with a single-phase fluid with viscosity $\mu = 0.0981$cP, and with a Biot modulus $M = 5.44 \cdot 10^{-6}$1/bar and a tensor of Biot coefficients equal to the identity matrix $B = I$. The load $F = 10$ MPa is applied to the initially undeformed domain with $p^0 = 0$.

Fig. 10 depicts a comparison of pressures for the numerical and analytical solutions. Time is expressed in dimensionless form as $t_D = \frac{L^2\mu}{kM}\frac{K_d + 4/3G + b^2M}{K_{dr} + 4/3G}$, where $k = k_x$ is the scalar permeability, L is the horizontal extent of the domain, K_d is the drained bulk modulus, G is the drained shear modulus, $b = 1$ is the scalar Biot coefficient, M is the Biot modulus, and μ is fluid viscosity. Pressure is normalized with respect to half the applied load. The calculated pressure distribution over the entire domain is depicted in Fig. 11.

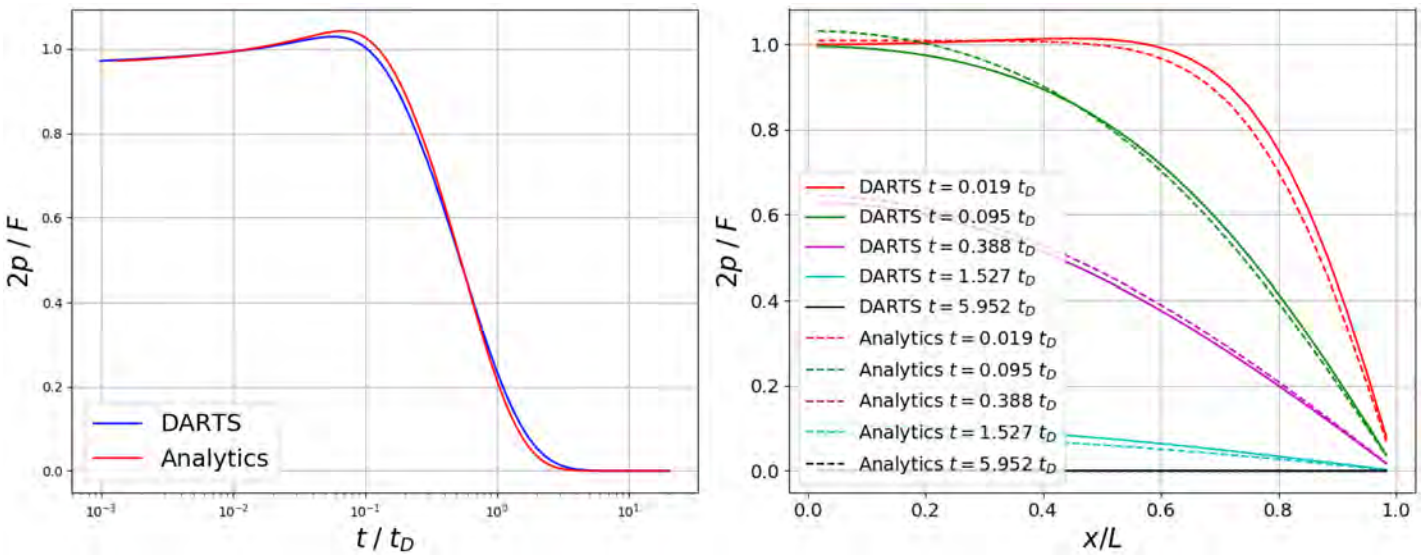

Figure 10—Comparison of calculated pressure (DARTS) with analytical solution. Normalized pressure at the left bottom cell over time (left) and normalized pressure along horizontal centerline at different moments of time.

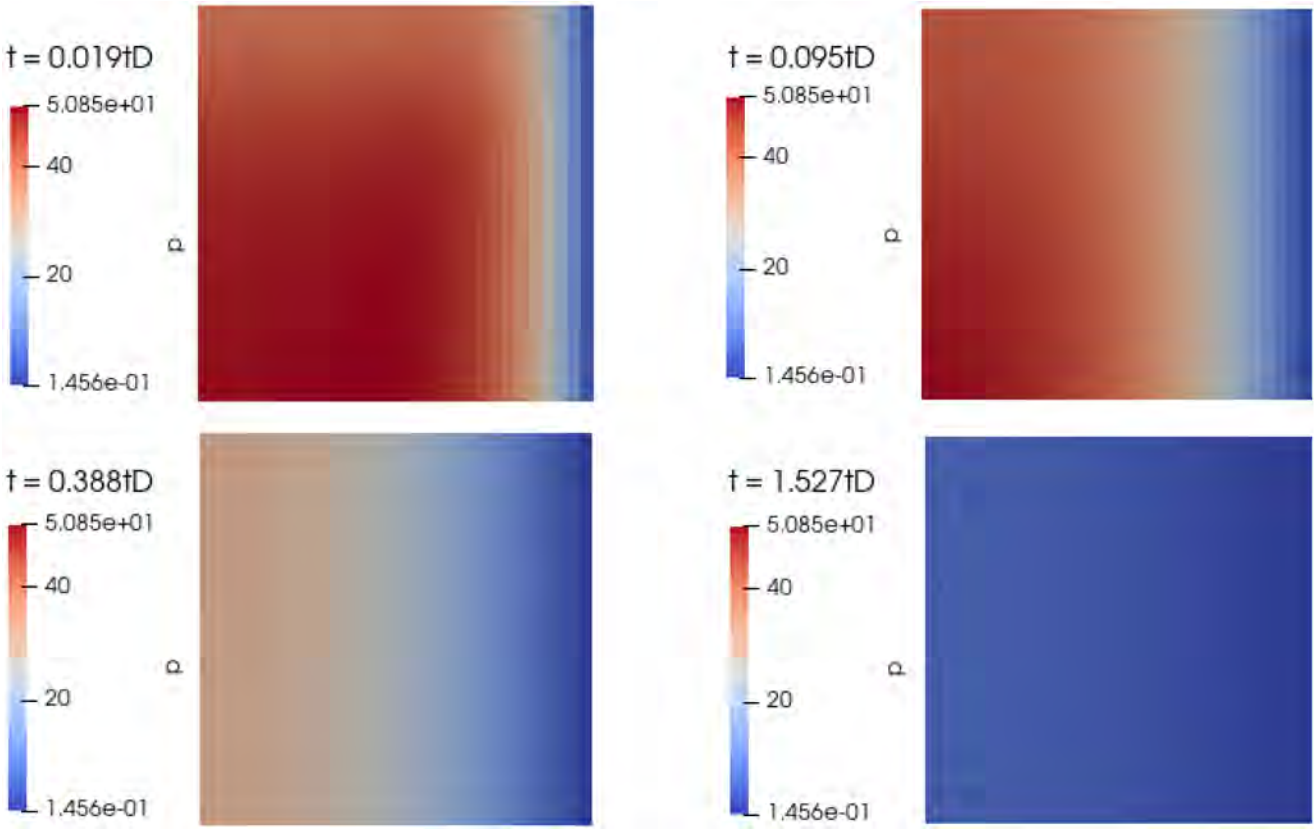

Figure 11—Pressure over domain in bars at different moments of time.

The efficiency of fixed-stress block-partitioned preconditioning strategy is tested in the Mandel problem. The results are presented in Table 6.

Table 6—Speed up obtained using fixed-stress preconditioning compared with an ILU0 preconditioner for the full system. TS – time steps, NI – non-linear iterations, LI – linear iterations.

Nr. of cells	Preconditioner	Nr. of TS	Nr. of NI	Nr. of LI	Solver time, s.
5400	ILU0	20	20	8547	28.73
5400	fixed-stress	20	20	328	11.1

SPE 10 Mechanical Extension

In this test case we use data from the SPE10 benchmark for flow supplemented by mechanical parameters, in particular a spatial distribution of Young's modulus that depends linearly on the porosity (Garipov et al., 2018). The original dataset represents a reservoir characterized by a channelized permeability and by a permeability field that has a Gaussian spatial covariance; see Fig. 12. The dataset was coarsened using a volume-averaging approach (Garipov et al., 2018). Although the original SPE10 benchmark was designed as a two-phase flow problem, here we consider single-phase flow. The reservoir is produced by a single doublet of an injector and a producer. No-flow boundary conditions are prescribed for all the boundaries. Normal displacements and tangential tractions are set to zero at all boundaries except for the top boundary where a uniform distributed load of 900 bar is applied. Poisson's coefficient is taken as constant $\nu = 0.2$, and the Young's modulus and lateral permeability fields are depicted in Fig. 12.

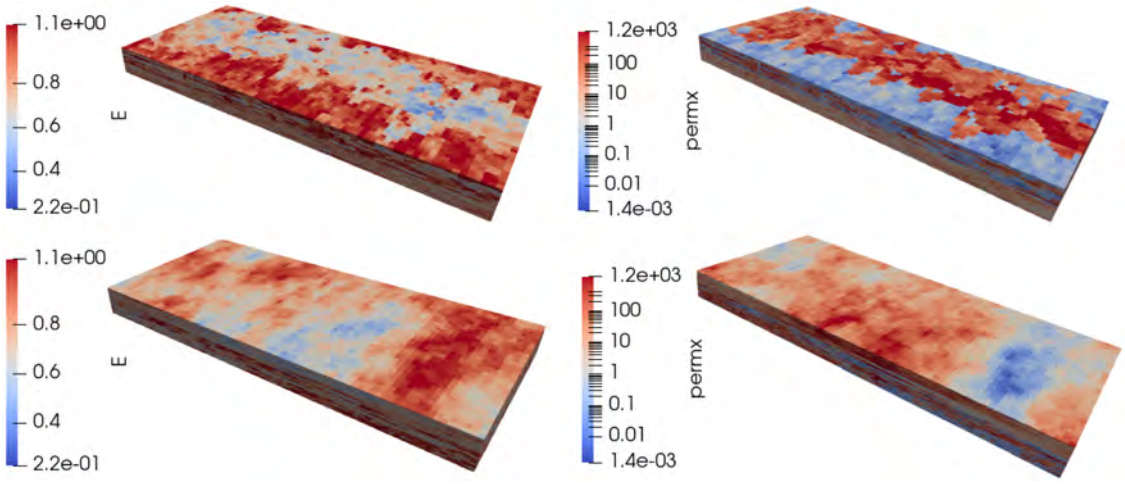

Figure 12—Young modulus (in GPa) and lateral permeability (in mDa) fields shown from the top (top row) and from the bottom (bottom row) of reservoir. Young modulus is calculated as a linear function of porosity. Top 24 layers represent channelized structure whereas bottom 16 layers correspond to Gaussian distribution.

The calculations are made using three rectangular grids of different resolutions: 20 × 40 × 20, 40 × 80 × 20, 40 × 80 × 40. Constant bottom hole pressures are kept at producer $p_{prod} = p^0 - 100$bar and injector $p_{inj} = p^0 - 100$bar wells for $t_{max} = 2$ years. The results are summarized in Fig. 13. They demonstrate applicability of block-partitioned preconditioning for the solution of discrete system produced by coupled FVM multi-point scheme.

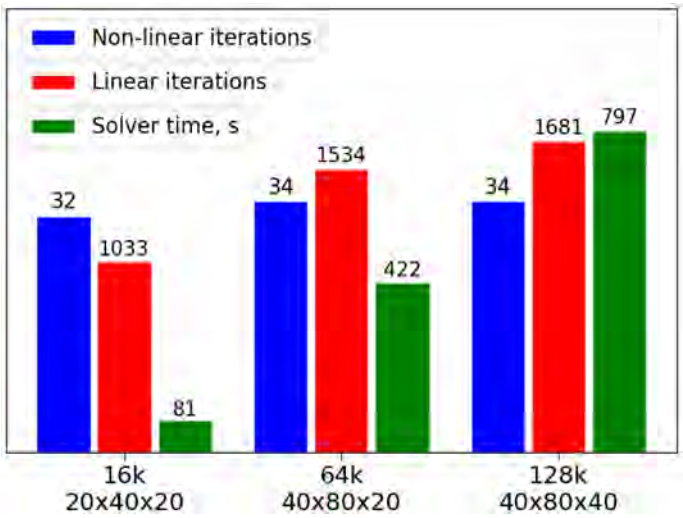

Figure 13—Cumulative number of non-linear iterations, linear iterations and computational time taken by linear solver to calculate 20 time steps for the model of three different resolutions.

LBB-Instability

In the the original test case reported by Terekhov (2020a), the FV approximation showed a divergent solution for very small time steps. In our implementation we observed unstable behavior for small time steps as well. In Fig. 14 the evolution of the discrepancy between true and computed solutions is depicted. The setup was taken from Test Case 1 and was calculated using an 8 × 8 × 8 cubic grid for a time period $t \in [0,0.01]$ days.

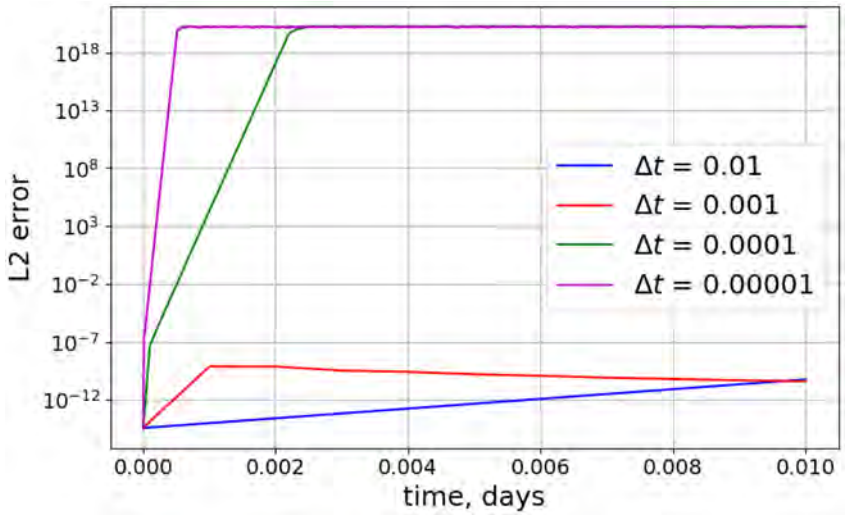

Figure 14—L2 norm of the difference between computed and true solutions over time. The setup is the taken from Test Case 1. Calculations were made with different time steps with magnitude Δt = 0.01, 0.001, 0.0001 and 0.00001 d. Below a certain time step size the error increases sharply.

For calculations made with $\Delta t = 0.01$ and $\Delta t = 0.001$ the discrepancy remains at the level of machine precision whereas for smaller time steps it rises drastically.

Such behavior is explained by the violation of inf-sup stability condition which is also known as Ladyzhenskaya–Babuska–Brezzi (LBB) condition which is a sufficient condition for a saddle point problem to have a unique solution (Shinbrot, 1971). The saddle point appears in our numerical scheme because matrices A_i and A_j defined in equation (21) have eigenvalues of different signs. The occurrence of the saddle point can be avoided by introducing a stabilization term into the matrices (Terekhov, 2020b).

Conclusion

We have developed a collocated Finite Volume Method with a multi-point approximation of fluxes for geomechanics and poromechanics. The method can cope with discontinuities in displacements, as occur in faults, on the level of discretization. Building on earlier work by Terekhov and Tchelepi (2020) and Terekhov (2020a,b), we introduced gap degrees of freedom over the fault which significantly simplified the formulation of contact conditions. We validated the method against several analytical and numerical solutions in a number of different test cases.

The multi-point stress discretization behaves robustly on structured corner-point grids but can exhibit oscillations on unstructured simplex and hexahedral grids. This issue can be resolved by the extension of the stencil used for gradient reconstruction by using the concept of homogenezation functions (Terekhov et al., 2017) or with a dual grid formulation (Keilegavlen and Nordbotten, 2017). We aim to address this issue in future work. Moreover we foresee an extension of our methodology for compositional flow in poroelastic media.

Nomenclature

Physical Variables

p – pore pressure,
φ – porosity,
$\widetilde{\phi} = \phi^0 + (p - p^0)(b - \phi^0)/K_s$,
ρ – fluid density,
μ – fluid viscosity,

$\mathbf{v}$ – Darcy's velocity of fluid,
f – sources (or sinks) of fluid mass,
K – rank-two tensor of permeability,
k_x, k_y, k_z – diagonal components of permeability tensor,
g – gravity constant,
z – depth,
σ – total stress tensor,
$\mathbf{f}$ – volumetric forces applied to the medium,
$\mathbb{C}$ – rank-four stiffness tensor of skeleton,
C – 6 × 6 symmetric matrix of stiffness coefficients,
ε – strain tensor,
$\varepsilon_V =$ tr(ε) – volumetric strain,
B – 2nd rank tensor of Biot's coefficients,
$b = 1 - K_d/K_s$ – Biot's coefficient,
$K_d \approx \frac{1}{9} I : \mathbb{C} : I$ – bulk modulus of the drained skeleton,
K_s – bulk modulus of the solid phase,
M – Biot's modulus,
$\mathbf{n}$ – unit normal vector,
$\mathbf{u}$ – vector of displacement,
$\mathbf{u}^-, \mathbf{u}^-$ – displacements at the particular side of the fault,
$\mathbf{g}$ – 3 × 1 vector of gap in displacements or 4 × 1 vector $\{\mathbf{g}, 0\}$,
$g_N, \mathbf{g}_T$ – normal and tangential projections of gap vector,
$\mathbf{F}$ – traction vector,
$F_N, \mathbf{F}T$ – normal and tangential projections of traction vector,
$\mathbf{F}'$ – effective traction vector,
$F'_N, \mathbf{F}'_T$ – normal and tangential projections of effective traction vector,
q – fluid flux,
$\tilde{q}$ – flux of displacement,
$q_t = q + \partial\tilde{q}/\partial t$ – total fluid flux, i.e. taking into account structure movement,
ν – Poisson's ratio,
η – friction coefficients,
$\Phi = |\mathbf{F}'_T| - \eta F'_N$ – Coulomb function
E – Young's modulus,
t – time,
I – identity matrix

Numerical Variables

$\mathbf{w} = \{\mathbf{u}, p\}$ – vector of unknowns,
$\mathbf{x}_i$ – ith cell center,
$\mathbf{x}_\delta$ – center of the interface
$\mathbf{y}_i$ – projection of the ith cell center on interface,
r_i – distance between ith cell center and interface,
δ_j – area of jth interface,
V_i – volume of ith cell,
Δt – time step size,

Y – 9 × 6 matrix,
S_i – 9 × 9 matrix,
$\mathbf{G}_i, \mathbf{G}_{\tau i}$ – 4 × 1 and 12 × 1 vectors of normal and tangential projections of the gradients of unknowns in *i*th cell,
T_i, Γ_i – 3 × 3 and 3 × 9 matrices,
λ_i, γ_i – normal and tangential projections of co-normal permeability vector,
A_i, Q_i – 4 × 4 matrices,
Θ_i – 4 × 12 matrix,
$\mathbf{R}_i$ – 4 × 1 vector,
J – jacobian matrix,
$J_{uu}, J_{up}, J_{pu}, J_{pp}$ – blocks of globally-partitioned Jacobian matrix,
S_{pp} – Schur's complement of of J_{uu} in Jacobian matrix,
P_u^{-1}, P_p^{-1} – preconditioners used for displacement and pressure blocks of Jacobian matrix

References

Ambartsumyan, I., Khattatov, E., Nordbotten, J. M., and Yotov, I. (2020). A multipoint stress mixed finite element method for elasticity on simplicial grids. *SIAM Journal on Numerical Analysis*, **58**(1):630–656.

Arbogast, T., Wheeler, M. F., and Yotov, I. (1997). Mixed finite elements for elliptic problems with tensor coefficients as cell-centered finite differences. *SIAM Journal on Numerical Analysis*, **34**(2):828–852.

Arnold, D., Falk, R., and Winther, R. (2007). Mixed finite element methods for linear elasticity with weakly imposed symmetry. *Mathematics of Computation*, **76**(260):1699–1723.

Berge, R. L., Berre, I., Keilegavlen, E., Nordbotten, J. M., and Wohlmuth, B. (2020). Finite volume discretization for poroelastic media with fractures modeled by contact mechanics. *International Journal for Numerical Methods in Engineering*, **121**(4):644–663.

Buijze, L., van den Bogert, P., Wassing, B., and Orlic, B. (2019). Nucleation and arrest of dynamic rupture induced by reservoir depletion. *Journal of Geophysical Research: Solid Earth*, **124**(4):3620–3645.

Coussy, O. (2003). *Thermoporoelasticity*, chapter 4, pages 71–112. John Wiley & Sons, Ltd.

Deb, R. and Jenny, P. (2017a). Finite volume–based modeling of flow-induced shear failure along fracture manifolds. *International Journal for Numerical and Analytical Methods in Geomechanics*, **41**(18):1922–1942.

Deb, R. and Jenny, P. (2017b). Modeling of shear failure in fractured reservoirs with a porous matrix. *Computational Geosciences*, **21**(5-6):1119–1134.

Garipov, T. and Hui, M. (2019). Discrete fracture modeling approach for simulating coupled thermo-hydro-mechanical effects in fractured reservoirs. *International Journal of Rock Mechanics and Mining Sciences*, 122.

Garipov, T., Karimi-Fard, M., and Tchelepi, H. (2016). Discrete fracture model for coupled flow and geomechanics. *Computational Geosciences*, **20**(1):149–160.

Garipov, T., Tomin, P., Rin, R., Voskov, D., and Tchelepi, H. (2018). Unified thermo-compositional-mechanical framework for reservoir simulation. *Computational Geosciences*, **22**(4):1039–1057.

Jansen, J., Singhal, P., and Vossepoel, F. (2019). Insights from closed-form expressions for injection-and production-induced stresses in displaced faults. *Journal of Geophysical Research: Solid Earth*, **124**(7):7193–7212.

Jha, B. and Juanes, R. (2014). Coupled multiphase flow and poromechanics: A computational model of pore pressure effects on fault slip and earthquake triggering. *Water Resources Research*, **50**(5):3776–3808.

Kala, K. and Voskov, D. (2020). Element balance formulation in reactive compositional flow and transport with parameterization technique. *Computational Geosciences*, **24**(2):609–624.

Keilegavlen, E., Berge, R., Fumagalli, A., Starnoni, M., Stefansson, I., Varela, J., and Berre, I. (2021). Porepy: an open-source software for simulation of multiphysics processes in fractured porous media. *Computational Geosciences*, **25**(1):243–265.

Keilegavlen, E. and Nordbotten, J. (2017). Finite volume methods for elasticity with weak symmetry. *International Journal for Numerical Methods in Engineering*, **112**(8):939–962.

Khait, M. and Voskov, D. (2018a). Adaptive parameterization for solving of thermal/compositional nonlinear flow and transport with buoyancy. *SPE Journal*, **23**(2):522–534.

Khait, M. and Voskov, D. (2018b). Operator-based linearization for efficient modeling of geothermal processes. *Geothermics*, **74**:7–18.

Kim, J., Tchelepi, H., and Juanes, R. (2011). Stability and convergence of sequential methods for coupled flow and geomechanics: Fixed-stress and fixed-strain splits. *Computer Methods in Applied Mechanics and Engineering*, **200**(13-16):1591–1606.

Klevtsov, S., Castelletto, N., White, J., and Tchelepi, H. (2016). Block-preconditioned krylov methods for coupled multi-phase reservoir flow and geomechanics.

Lyu, X., Khait, M., and Voskov, D. (2021a). Operator-based linearization approach for modelling of multiphase flow with buoyancy and capillarity. *SPE Journal*.

Lyu, X., Voskov, D., and Rossen, W. R. (2021b). Numerical investigations of foam-assisted co2 storage in saline aquifers. *International journal of greenhouse gas control*.

Nordbotten, J. (2014). Cell-centered finite volume discretizations for deformable porous media. *International Journal for Numerical Methods in Engineering*, **100**(6):399–418.

Phillips, P. and Wheeler, M. (2007). A coupling of mixed and continuous galerkin finite element methods for poroelasticity i: The continuous in time case. *Computational Geosciences*, **11**(2):131–144.

Settari, A. and Mourits, F. (1998). A coupled reservoir and geomechanical simulation system. *SPE Journal*, **3**(3):219–226.

Shinbrot, M. (1971). The mathematical theory of viscous incompressible flow (O. A. Ladyzhenskaya). *SIAM Review*, **13**(1):103–106.

Sokolova, I., Bastisya, M., and Hajibeygi, H. (2019). Multiscale finite volume method for finite-volume-based simulation of poroelasticity. *Journal of Computational Physics*, **379**:309–324.

Terekhov, K. (2020a). Cell-centered finite-volume method for heterogeneous anisotropic poromechanics problem. *Journal of Computational and Applied Mathematics*, 365.

Terekhov, K. (2020b). Multi-physics flux coupling for hydraulic fracturing modelling within inmost platform. *Russian Journal of Numerical Analysis and Mathematical Modelling*, **35**(4):223–237.

Terekhov, K., Mallison, B., and Tchelepi, H. (2017). Cell-centered nonlinear finite-volume methods for the heterogeneous anisotropic diffusion problem. *Journal of Computational Physics*, **330**:245–267.

Terekhov, K. and Tchelepi, H. (2020). Cell-centered finite-volume method for elastic deformation of heterogeneous media with full-tensor properties. *Journal of Computational and Applied Mathematics*, 364.

Wang, Y., Voskov, D., Khait, M., and Bruhn, D. (2020). An efficient numerical simulator for geothermal simulation: A benchmark study. *Applied Energy*, 264.

White, J., Castelletto, N., and Tchelepi, H. (2016). Block-partitioned solvers for coupled poromechanics: A unified framework. *Computer Methods in Applied Mechanics and Engineering*, **303**:55–74.